Diffraction Enhanced Imaging Utilising a Laser Produced X-ray Source

M. Oliver,[1,2,a)] C. H. Allen,[2] L. Divol,[3] Z. Karmiol,[2] O. Landen,[3] Y. Ping,[3] R. Wallace,[3] M. Schölmerich,[3] W. Theobald,[4] T. Döppner,[3] and T. G. White[2]
[1)]*Rutherford Appleton Laboratory, Didcot OX11 0DE.*
[2)]*University of Nevada, Reno. 1664 N Virginia St, Reno, NV 89557.*
[3)]*Lawrence Livermore National Laboratory, L-493, 70000 East Avenue, Livermore, CA 94550.*
[4)]*Laboratory for Laser energetics, 250 E River Rd, Rochester, NY 14623*

(Dated: 13 January 2023)

Image formation by Fresnel diffraction utilizes both absorption and phase-contrast to measure electron density profiles. The low spatial and spectral coherence requirements allow the technique to be performed with a laser-produced X-ray source coupled with a narrow slit. This makes it an excellent candidate for probing interfaces between materials at extreme conditions, which can only be generated at large-scale laser or pulsed power facilities. Here we present results from a proof-of-principle experiment demonstrating an effective ~ 2 μm laser-generated source at the OMEGA laser facility. This was achieved using slits of 1 μm $\times$ 30 μm and 2 μm $\times$ 40 μm geometry, which were milled into 30 μm thick Ta plates. Combining these slits with a vanadium He-like 5.2 keV source created a 1-D imaging system capable of micron-scale resolution. The principal obstacles to achieving an effective 1 μm source are the slit tilt and taper - where the use of a tapered slit is necessary to increase the alignment tolerance. We demonstrate an effective source size by imaging a 2 ± 0.2 μm radius tungsten wire.

I. INTRODUCTION

X-ray imaging is ubiquitous with the study of extreme matter states such as those created in shock compression[1] and inertial confinement fusion[2–4]. High spatial resolution images are frequently obtained using phase contrast techniques that rely on generating a spatially coherent x-ray source, e.g., a free-electron laser or a betatron source, with typical source sizes on the order of $\sim$1 μm[1,5,6]. However, most high-power laser facilities rely on laser-driven solid targets to create x-ray probe beams. A crucial limiting factor in image resolution is the source size; thus, pinholes or slits are used to reduce the effective size of the x-ray source. Previously, spatial resolutions down to $\sim$5 μm have been achieved in x-ray radiography using laser-milled slits[7–9] or thin wire targets[10].

Here, we present diffraction patterns of cylindrical targets at ambient conditions imaged using laser-produced X-ray sources with slit widths down to 1 μm. By utilizing these novel 1 μm wide slits, five times smaller than previously demonstrated, we obtain a highly spatially coherent x-ray source that gives rise to significant refractive and diffractive features from micron-scale density gradients. With the correct geometry, this provides a wealth of information that standard radiography setups obscure. To demonstrate the efficacy of the technique and the effective source size achieved, we compare the experimental results to synthetic diffraction patterns. We also discuss the determination of temporally and energetically resolved X-ray source spectra required to predict the diffraction pattern and accurately extract physical information.

In planned dynamic experiments, the capability to measure density gradients on micron-level spatial scales provides exciting opportunities to directly investigate the effects of transport properties in warm dense matter[11], such as mutual diffusion and thermal conductivity, which act to modify the scale-length at the interface between two different materials. Furthermore, the significantly smaller source size and improved imaging geometry will enhance the measurement of density profiles across shocks and interfaces more generally.

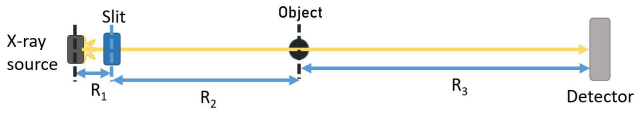

FIG. 1. Schematic illustrating the diagnostic setup. R_1 is the distance between the source and the slit, R_2 is the distance between the slit and the object to be imaged, and R_3 is the distance between the object and the detector. The magnification of the setup is given by R_3/R_2.

II. FRESNEL DIFFRACTION IMAGING

Image formation by Fresnel diffraction is an absorption-contrast and phase-contrast-based technique[12] sensitive to density gradients within the probed sample. The diagnostic setup has a similar geometry to standard radiography, see Figure 1.

The required spatial coherence of the source is accomplished with a $\sim$1 μm wide slit, milled using a focused ion beam (FIB). The slit provides spatial coherence along one axis direction while allowing integration along the other to increase the signal-to-noise.

An excellent and comprehensive description of Fresnel diffractive imaging can be found in the work of Pogany *et al.* who developed a framework for hard x-ray phase-contrast microscopy and imaging[12]. The source-to-object distance (R_2) and probe wavelength (λ) determine which feature size receives optimum contrast. For example, for features of order s = 2 μm and a λ = 2 Å source, this occurs for $R_2 = s^2/2\lambda$

[a)]Electronic mail: matthew.oliver@stfc.ac.uk

= 10 mm. The object to screen distance (R_3) is chosen to provide the required magnification ($M = R_3/R_2$), whilst also maintaining the required signal level on the detector.

The spatial-coherence requirement for diffraction-based imaging constrains the size of the slit. Here, the primary factor for spatial coherence is the source size, related to the slit width. In order to observe the diffraction pattern imprinted by an object, a source size ζ less than twice the location of the first maximum in the diffraction pattern (projected back to the object) is required[13]. In the case of a 2 μm object, this is approximately given by,

$$\zeta < 2 \times 0.7 \sqrt{\frac{R_2 R_3 \lambda}{2(R_2 + R_3)}} = 1.4\ \mu m \qquad (1)$$

for R_3 = 1000 mm. Cutting a < 2 μm slit through a plate of thickness on the order of tens-of-microns is not achievable using traditional laser milling techniques[8]. Therefore, we create the slits using a focused ion beam. Scanning electron microscopy (SEM) images of a typical slit are shown in Figure 2. The slits were prepared using a Thermo Scientific Scios2 DualBeam microscope. This instrument uses gallium ions for focused ion beam milling, with variable voltages and currents allowing for the tapered geometry of the incident side of the slit, and to ensure that the exit geometry adhered to the specified requirements.

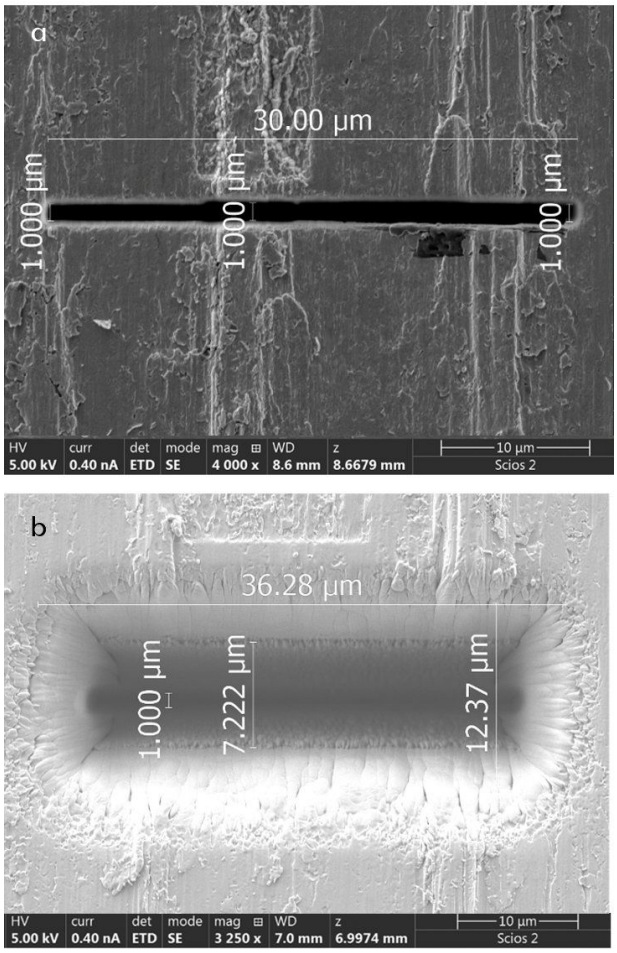

FIG. 2. Scanning electron microscope images of the slit. (a) 1 μm × 30 μm slit exit aperture. (b) 10 μm × 30 μm slit entrance aperture. The slit was milled using a focused ion beam at the University of Nevada, Reno. The slit tapers from 1 μm × 30 μm (a) to 10 μm × 30 μm (b) in a 30 μm thick Ta plate. The taper increases alignment tolerances, ensuring a strong signal through the slit, even if the slit plate is slightly rotated.

III. EXPERIMENTAL DESIGN

A. Experimental setup

The experiment was performed at the OMEGA laser at the Laboratory for Laser Energetics (LLE) of the University of Rochester[15]. We trialed two different target setups: a monolithic target and a three stalk target. For the monolithic setup[14], shown in Figure 3a, the slit and wire target were held together by a large 3D printed scaffold. This enabled the slit and diffraction target to be co-aligned prior to insertion into the target chamber. For the three stalk target, shown in Figure 3b, the two components were co-aligned within the target chamber using the target positioning cameras.

For each target type, a 7 $\pm$ 2 μm vanadium foil was irradiated with 8 - 10 1 ns, $\sim$ 450 J, 351 nm laser beams to generate a He-like 5.2 keV X-ray probe. To ensure full illumination on the detector, spot diameters $\geq$ 350 μm were utilized. The X-rays passed through a tapered slit milled in a 30 μm thick, 10 mm × 10 mm area tantalum plate located on axis 5 mm or 10 mm away from the vanadium foil. In both cases, the wider side of the taper was directed towards the X-ray source. Images of a slit taken using a scanning electron microscope are shown in Figure 2. The slit was filled with CH foam in order to slow the expansion of the Ta caused by x-ray heating and thus decrease the rate of slit closure. Two slit sizes were utilized. On the monolithic setup, the slit tapered from 10 μm × 40 μm to 2 μm × 40 μm. On the three stalk setup, the slit tapered from 10 μm × 30 μm to 1 μm × 30 μm. The slit taper was crucial to increase the angular tolerance during alignment. Without the a taper in the slit, even a 1 degree rotation would substantially reduce the X-ray signal which passes through the slit.

The slit was milled at the center of four 150 μm diameter alignment holes laser cut into the tantalum plate; these holes were large enough to be visible on the in chamber target alignment system. A fifth 150 μm diameter hole was used to break the symmetry, enabling the direction of the taper to be independently defined. A schematic of the slit plate is given in the Supplementary Information. The slit and backlighter foil were both tilted by 20 degrees as shown in figure 3 in order to prevent damage to diagnostics from target debris. Twenty microns of Polypropylene at a density of 0.9 g/cc CH was used to fill the tapered slit. X-rays that passed through the slit illuminated the diffraction target located either 13 mm or 15 mm from the slit. The image was recorded on an X-ray framing camera (XRFC) placed 1 m from the diffraction target. The

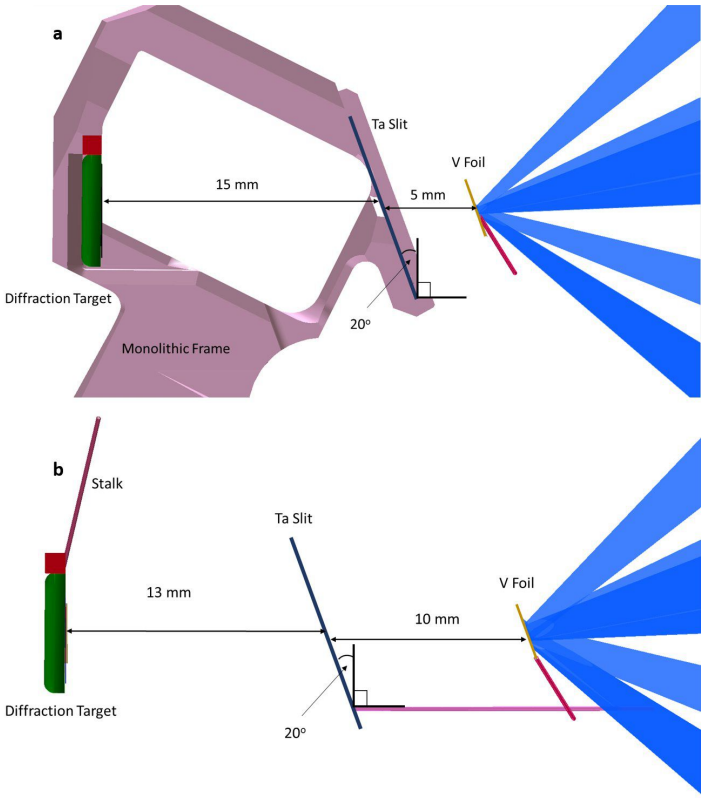

FIG. 3. Diagram of the experimental setup. (a) Monolithic target design (see also[14]). A 3D printed holder enables the slit and diffraction target to be aligned offline before the experiment. The diffraction target consisted of a 4 μm diameter tungsten wire supported in a plastic frame 15 mm from the 2 μm $\times$ 40 μm slit. (b) Three stalk target design. The slit and diffraction target are co-aligned in the vacuum chamber before a shot. In both cases, the diffraction target consisted of a 4 μm diameter tungsten wire.

XRFC consisted of two multi-channel plate (MCP) detector strips that were operated with a 500 ps pulse forming module resulting in a 240 ps integration time[16,17]. The camera had a pixel size of 18 μm$\times$18 μm. For some shots, part of the XRFC was covered with BAS-SR image plate[18,19] scanned with a resolution size of 25 μm$\times$25 μm to assist with initial target alignment.

For the monolithic target design, the XRFC contained a filter pack consisting of 8 materials used to determine the approximate spectrum of X-rays (see the Supplementary Information). The detector region containing the image of the buried wire was filtered with 10 μm thick vanadium. The laser energy on the vanadium backlighter foil was $\sim$ 4500 J with a laser-spot diameter of $\sim$ 350 μm. For the three stalk target, the corresponding filter pack on the XRFC contained a Ross pair which allowed the signal outside of a narrow band between 4.8 keV and 5.2 keV to be subtracted from the data. The laser drive energy incident on the vanadium backlighter foil was $\sim$ 3500 J with a laser-spot diameter of $\sim$650 μm. In both cases, the diffraction target consisted of a 4$\pm$0.4 μm diameter tungsten wire.

B. Diffraction through the slit

The minimum size of the slit perpendicular to R_2 is of the order of a micron. Given that, it will, of course, also diffract the transmitted X-rays. The calculated diffraction parameter for the setup described above is $\sqrt{R_1\lambda}$ = 1.1 μm, where R_1 = 5 mm. This is similar to the slit width $\sim$1 μm, thus the system will be in the Fresnel regime with diffraction angles of the order of 2.4 Å/1 μm $\sim$ 0.2 mrad. However, the slit (even accounting for its 30 μm thickness) will transmit a broad range ($\sim$ 0.1 rad) of photon angles from a typical 350 μm backlighter source size, which will result in complete blurring of the slits diffraction pattern. Thus, the slit can be considered to produce a spatially coherent point-like source with a source spread function along the imaging axis of $\sim$ 1 μm.

C. Slit closure

X-rays from the backlighter source may heat the slit plate and reduce the effective slit size during the experiment[20]. To check for slit closure, we compared the signal levels on the image plate for both 1 $\times$ 30 μm and 2 $\times$ 40 μm slits. Hard X-rays that pass through the Ta plate ($\gtrsim$ 10 keV) form a spatially flat featureless background. Thus, by comparing the amplitude of the images of the W wire formed by the different sized slits, we can approximate the ratio of the transmitted intensities. This provides an estimate of the effective area of the two slits and gives an indication of if there was significant slit closure. The spatiotemporally integrated images for both slit sizes are shown in Figure 4. As the transmission through the W wire is only 2 % for 5.2 KeV x-rays, we set intensity of the image minima to zero to account for background sources such as X-rays that have passed through the slit plate. The ratio of the two signals is $\sim$ 0.4 $\pm$ 0.1, which is similar to the ratio of the two-slit areas = 0.375. This suggests that the slits did not close significantly over the duration of the backlighter emission ($\sim$1 ns).

IV. RESULTS: COMPARISON BETWEEN SYNTHETIC AND EXPERIMENTAL DIFFRACTION PATTERNS

To take advantage of the 1D nature of the imaging, the XRFC image is integrated parallel to the axis of each wire. In addition, the diffraction pattern of the wire is assumed to be symmetric. Therefore, to maximize the signal-to-noise, each wire's image is reflected along its center and added to the original image; this effectively doubles the integration area. An example of the XRFC data is shown above in figure 6. Figure 6a shows the 2D image of the wire on the framing camera. Figure 6b shows the vertically averaged data as well as the axially mirrored data and the average of the two. The large scale background gradient across the camera has been removed in the lineouts. As can be seen in figure 6b the data is highly symmetric about the wire axis and therefore mirroring the data and taking the average does not have a significant effect on the lineout which is used in the fitting process.

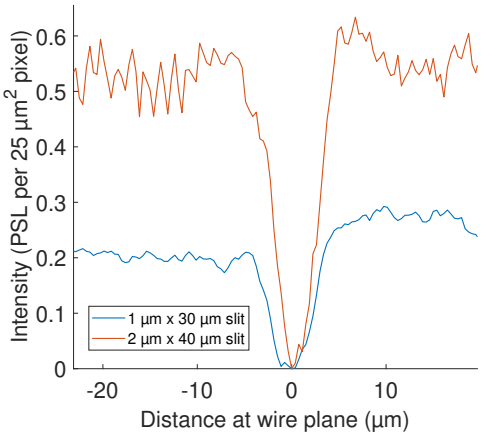

FIG. 4. Image plate data showing the amplitude of the image formed for both the 1 and 2 μm slit. Blue curve: 1×30 μm. Orange curve 2×40 μm.

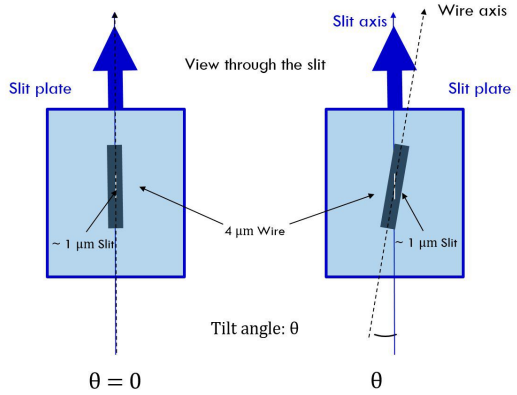

FIG. 5. Schematic defining slit tilt, not to scale. A relative tilt between the wire axis and the slit axis results in a source broadening.

To generate the synthetic diffraction patterns, we assume a cylindrically symmetric target and use the complex transmission function together with the Fresnel–Kirchhoff integral. Details of the calculation can be found in Pogany *et al*[12]. The corresponding experimental geometries are shown in Figure 3. In the experiment, as the slit is > 10X longer than it is wide, any tilt between the axis of the slit and the axis of the wire, (see Figure 5) induces additional source broadening. The exact source shape is given by the vertical projection of the tilted slit and this must be taken into account when generating the synthetic diffraction patterns.

Furthermore, as the attenuation length of 5.2 keV X-rays in Ta is 1.25 μm, the shape of the source itself is sensitive to the shape of the taper running through the plate. Whilst it was possible to measure the exterior slit width on both sides of the Ta foil, see Figure 2, we were unable to measure the profile of the taper through the plate. Thus, calculations were performed over a range of relative tilts and slit tapers for comparison to the data. Various shaped slit tapers are parameterised through the use of a power law in the form, $y \sim x^a$, where x is the distance from the central axis of the slit, y is the thickness of the slit plate and a is the taper exponent. Figure 7 shows the slit shapes and the effective source shapes for a range of taper exponents. X-ray transmission through the tapering slit give rise to an effective source size that is always greater than the narrowest aperture of the of the slit.

Finally, we cannot distinguish between the signal that passes through the slit aperture and that which passes through the alignment holes. Thus, when fitting synthetic diffraction patterns to the experimental data, only the shape of the W wire rather than the absolute intensity is used. This allowed the fitting to be performed without knowledge of the intensity of any spatially large background across the detector due to either transmission through the slit plate or X-rays passing through the alignment holes.

A. Three Stalk Target

For this geometry (Figure 3b), data was collected ~700 ps after laser incidence on the backlighter foil, and we utilized the 1 μm×30 μm slit. As we aligned this target within the target chamber, the relative tilt between the slit and the wire could not be measured a-priori, thus demonstrating a disadvantage of this target type. A V/Ti Ross pair filter was utilized (7 μm V, 10 μm Ti). The subtracted Ross pair removed x-rays outside a narrow band between 4.8 keV and 5.4 keV, allowing diffraction simulations to be compared to the data without knowledge of the full emission spectra. Simulations were performed for a range of slit-wire tilt angles and slit tapers. A surface indicating the region of good fits is shown in Figure 8a. Figure 8b shows the simulated diffraction patterns for the three points marked on the surface while the corresponding source shapes are shown in Figure 8c. Each profile has a similarly good fit to the experimental data demonstrating that it is not possible to find the taper and tilt uniquely. However, they all exhibit a similar full width half maximum (FWHM). The FWHM of the three source shapes are 2.0 μm (tilt angle = 0.5°, taper exponent = 2), 2.5 μm (tilt angle = 3.5°, taper exponent = 1.5), and 2.5 μm (tilt angle = 5.0°, taper exponent = 0.5). Errors for the effective FWHM are found by varying the source tilt/taper until the simulated pattern no longer matches the data. This gives the source FWHM as 2.3 μm±0.5 μm. These error bounds are illustrated in Figure S4 the Supplementary Information.

B. Monolithic Target

For the monolithic target, data was taken ~800 ps after laser incidence on the backlighter foil. The relative tilt between the slit and the wire was found to be $1.7 \pm 1.0°$ during target characterization. Without the Ross pair, simulations of the diffraction pattern were performed with the full backlighter emission spectrum found in the Supplementary Information. A surface indicating the region of good fits is shown in Figure 9a. Figure 9b shows the simulated diffraction pat-

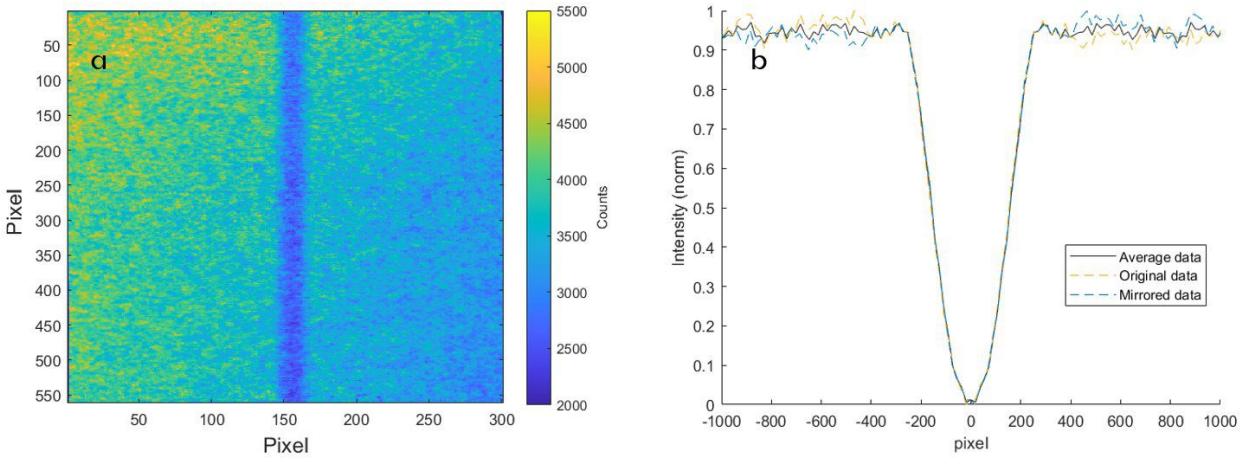

FIG. 6. Validation of the mirroring and averaging technique. (a) A 2D image of the W wire taken on the XRFC. (b) Integrated lineout of the wire with the large scale background removed. The data is highly symmetric about the wire axis.

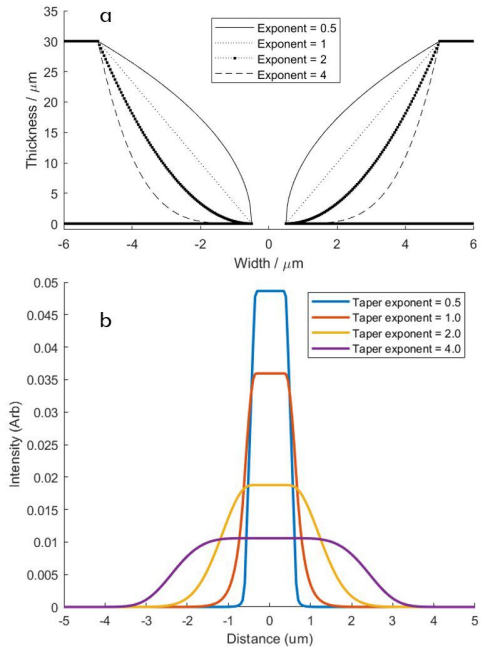

FIG. 7. (a) Various shaped slit tapers are parameterised through the use of a power law in the form, $y \sim x^a$, where x is the distance from the central axis of the slit, y is the thickness of the slit plate and a is the taper exponent. (b) The effective X-ray source shape for a 1 μm$\times$30 μm slit with a relative tilt of 0.5^o and taper exponents between 0.5 and 4.0. X-ray transmission through the narrowest part of the slit taper increases the effective source size.

terns for the three points marked on the surface while the corresponding source shapes are shown in Figure 9c. For the monolithic target, we only choose representative points on the surface that are consistent with the measured tilt. The FWHM of the three source shapes are 2.6 μm (tilt angle = 0.75^o, taper exponent = 1.5), 2.4 μm (tilt angle = 1.75^o, taper exponent = 1.25), and 2.4 μm (tilt angle = 2.75 ^{o}, taper exponent = 1.25). Again, we cannot determine the taper and tilt uniquely. However, the FWHM of the three sources are again very similar. Errors for the effective FWHM are found by varying the source tilt/taper until the simulated pattern no longer matches the data. This gives the source FWHM as 2.5 μm$\pm$0.6 μm. These error bounds are illustrated in figure S5 in the Supplementary Information.

Counter intuitively the FWHM of the sources are similar for both the 1 μm (2.3 μm $\pm$ 0.5 μm) and 2 μm slits, (2.5 μm $\pm$ 0.6 μm). This is because the the transmission through the tapered slit, and thus the effective source size, rely on the slit tilt, the exponent of the taper power law and the 10 μm width of the entrance aperture.

V. CONCLUSIONS AND FUTURE WORK

This experiment demonstrates the feasibility of utilizing a $\sim$ 1 μm slit to measure the profile of micron-scale objects using diffractive enhanced imaging. However, it has highlighted a number of technical issues. While the tilt between the slit and the diffraction target can be controlled with the monolithic target, the taper through the slit plate, essential for providing a reasonable alignment tolerance, makes it difficult to attain an effective sub-micron source size. To the knowledge of the authors, an effective source size of 2.3 μm $\pm$ 0.5 μm is the smallest laser-produced X-ray source size to date. In future work, a stepped slit as opposed to a continuous taper will be trialed in order to create a smaller effective source size while retaining acceptable alignment tolerance requirements. We will also seek to measure the modulation transfer function of the different slit sizes and attempt to reduce the relative tilt between the wire and the slit, building on the monolithic target design[14]. Future experiments will focus on driven/heated samples rather than stationary objects as well as focusing on more phase-driven, rather than absorption-driven, diffraction features.

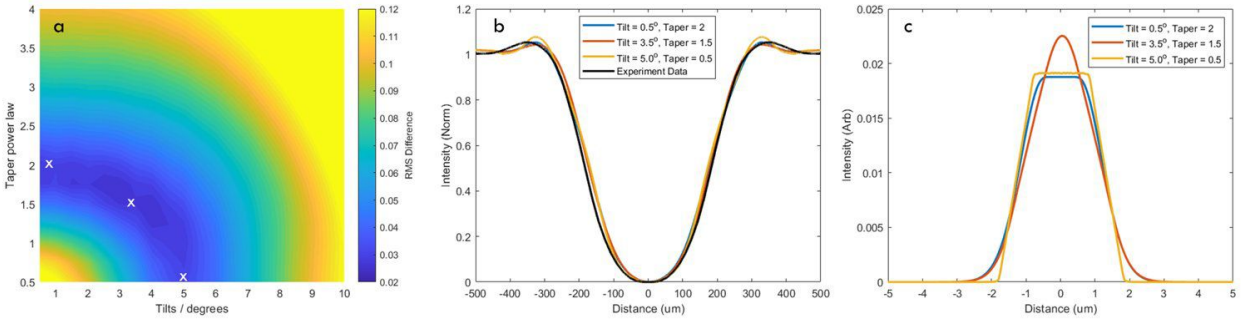

FIG. 8. Determination of the effective source size for the 4 μm W wire and 1 μm $\times$ 30 μm slit mounted in the three stalk target configuration. (a) A surface plot showing the region of taper-tilt combinations for which the calculated diffraction patterns match the experimental data. A range of taper-tilt combinations provide a good fit. The white crosses indicate the values of the taper and tilt used to perform the calculations plotted in Figures 8b and c. (b) A comparison between the experimental data and calculated diffraction patterns for the three tilt/taper combinations marked by the crosses in Figure 8a. (c) The shape and relative intensities of the X-ray source for the three taper/tilt combinations marked by the crosses in Figure 8a.

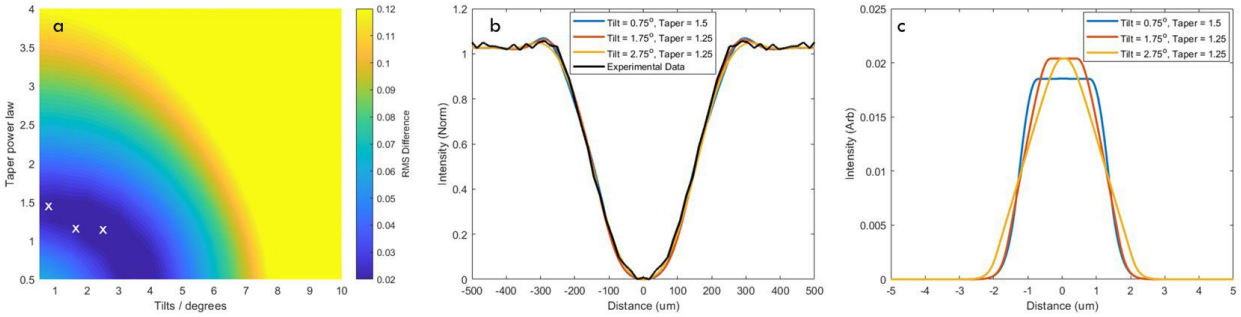

FIG. 9. Determination of the effective source size for the 4 μm W wire and 2 μm $\times$ 40 μm slit mounted on the monolithic target. (a) A surface plot showing the region of taper-tilt combinations for which the calculated diffraction patterns match the experimental data. A range of taper-tilt combinations provide a good fit. The white crosses indicate the values of the taper and tilt combinations used to perform the calculations plotted in Figures 9b and c. (b) A comparison between the experimental data and calculated diffraction patterns for the three tilt/taper combinations marked by the crosses in Figure 9a. (c) The shape and relative intensities of the X-ray source for the three taper/tilt combinations marked by the crosses in Figure 9a.

VI. SUPPLEMENTARY MATERIAL

The supplementary information describes the analysis performed to calculate the backlighter emission spectrum used to generate synthetic diffraction patterns for the Monolithic target in section IV B. It also contains further information about target design and the data analysis.

ACKNOWLEDGMENTS

We thank Russ Wallace and Ted Baumann for all their help constructing and characterizing the targets at LLNL. We would also like to thank all of the OMEGA staff involved in preparing and fielding the experiments, particular thanks goes to Jim Tellinghusen and Steven Ivancic for diagnostic support.

The experiment was conducted at the Omega Laser Facility at the University of Rochester's Laboratory for Laser Energetics with the beam time through the Laboratory Basic Science (LBS) program.

The work of L.D., O.L.L., Y.P., M.S. and T.D. was performed under the auspices of the U.S. Department of Energy by Lawrence Livermore National Laboratory under Contract No. DE-AC52-07NA27344 and supported by Laboratory Directed Research and Development (LDRD) Grant No. 21-ERD-029. This material is based upon work supported by the National Science Foundation under Grant Number PHY-2045718.

VII. REFERENCES

[1] J. Wood, D. Chapman, K. Poder, N. Lopes, M. Rutherford, T. White, F. Albert, K. Behm, N. Booth, J. Bryant, *et al.*, "Ultrafast imaging of laser driven shock waves using betatron x-rays from a laser wakefield accelerator," Scientific Reports **8**, 1–10 (2018).

[2] R. Kodama, P. Norreys, K. Mima, A. Dangor, R. Evans, H. Fujita, Y. Kitagawa, K. Krushelnick, T. Miyakoshi, N. Miyanaga, *et al.*, "Fast heating of ultrahigh-density plasma as a step towards laser fusion ignition," Nature **412**, 798–802 (2001).

[3]R. Betti and O. Hurricane, "Inertial-confinement fusion with lasers," Nature Physics **12**, 435–448 (2016).
[4]A. Zylstra, O. Hurricane, D. Callahan, A. Kritcher, J. Ralph, H. Robey, J. Ross, C. Young, K. Baker, D. Casey, *et al.*, "Burning plasma achieved in inertial fusion," Nature **601**, 542–548 (2022).
[5]B. Nagler, A. Schropp, E. C. Galtier, B. Arnold, S. B. Brown, A. Fry, A. Gleason, E. Granados, A. Hashim, J. B. Hastings, *et al.*, "The phase-contrast imaging instrument at the matter in extreme conditions endstation at lcls," Review of Scientific Instruments **87**, 103701 (2016).
[6]A. Schropp, R. Hoppe, V. Meier, J. Patommel, F. Seiboth, Y. Ping, D. G. Hicks, M. A. Beckwith, G. W. Collins, A. Higginbotham, *et al.*, "Imaging shock waves in diamond with both high temporal and spatial resolution at an xfel," Scientific reports **5**, 1–8 (2015).
[7]Y. Ping, O. Landen, D. Hicks, J. Koch, R. Wallace, C. Sorce, B. Hammel, and G. Collins, "Refraction-enhanced x-ray radiography for density profile measurements at ch/be interface," Journal of Instrumentation **6**, P09004 (2011).
[8]E. Dewald, O. Landen, L. Masse, D. Ho, Y. Ping, D. Thorn, N. Izumi, L. Berzak Hopkins, J. Kroll, A. Nikroo, *et al.*, "X-ray streaked refraction enhanced radiography for inferring inflight density gradients in icf capsule implosions," Review of Scientific Instruments **89**, 10G108 (2018).
[9]J. A. Koch, O. L. Landen, B. J. Kozioziemski, N. Izumi, E. L. Dewald, J. D. Salmonson, and B. A. Hammel, "Refraction-enhanced x-ray radiography for inertial confinement fusion and laser-produced plasma applications," Journal of Applied Physics **105**, 113112 (2009).
[10]L. Antonelli, F. Barbato, D. Mancelli, J. Trela, G. Zeraouli, G. Boutoux, P. Neumayer, S. Atzeni, A. Schiavi, L. Volpe, *et al.*, "X-ray phase-contrast imaging for laser-induced shock waves," EPL (Europhysics Letters) **125**, 35002 (2019).
[11]P. Grabowski, S. Hansen, M. Murillo, L. Stanton, F. Graziani, A. Zylstra, S. Baalrud, P. Arnault, A. Baczewski, L. Benedict, *et al.*, "Review of the first charged-particle transport coefficient comparison workshop," High Energy Density Physics **37**, 100905 (2020).
[12]A. Pogany, D. Gao, and S. Wilkins, "Contrast and resolution in imaging with a microfocus x-ray source," Review of Scientific Instruments **68**, 2774–2782 (1997).
[13]G. Margaritondo and G. Tromba, "Coherence-based edge diffraction sharpening of x-ray images: a simple model," Journal of applied physics **85**, 3406–3408 (1999).
[14]C. ALLEN, M. OLIVER, L. DIVOL, O. LANDEN, Y. PING, M. SCHÖLMERICH, R. WALLACE, R. EARLEY, W. THEOBALD, T. WHITE, *et al.*, "Towards an integrated platform for characterizing laser-driven, isochorically-heated plasmas with 1 m spatial resolution," Applied Optics **61** (2022).
[15]T. R. Boehly, R. S. Craxton, R. J. Hutchison, J. H. Kelly, T. J. Kessler, S. A. Kumpan, S. A. Letzring, R. L. McCrory Jr, S. F. Morse, W. D. Seka, *et al.*, "Upgrade of the omega laser system," in *Solid State Lasers III*, Vol. 1627 (International Society for Optics and Photonics, 1992) pp. 236–245.
[16]J. Bateman, "The detection of hard x-rays (10–140 kev) by channel plate electron multipliers," Nuclear Instruments and Methods **144**, 537–545 (1977).
[17]J. A. Oertel, R. Aragonez, T. Archuleta, C. Barnes, L. Casper, V. Fatherley, T. Heinrichs, R. King, D. Landers, F. Lopez, *et al.*, "Gated x-ray detector for the national ignition facility," Review of scientific instruments **77**, 10E308 (2006).
[18]B. Maddox, H. Park, B. Remington, N. Izumi, S. Chen, C. Chen, G. Kimminau, Z. Ali, M. Haugh, and Q. Ma, "High-energy x-ray backlighter spectrum measurements using calibrated image plates," Review of Scientific Instruments **82**, 023111 (2011).
[19]J. Yan, J. Zheng, X. Zhang, L. Chen, and M. Wei, "Calibration of fuji bas-sr type imaging plate as high spatial resolution x-ray radiography recorder," in *Fourth International Symposium on Laser Interaction with Matter*, Vol. 10173 (International Society for Optics and Photonics, 2017) p. 101730V.
[20]A. Bullock, O. Landen, B. Blue, J. Edwards, and D. Bradley, "X-ray induced pinhole closure in point-projection x-ray radiography," Journal of applied physics **100**, 043301 (2006).